

## ARTICLE OPEN



# Characteristics and hot corrosion behavior of NiCrAlY metal bonding layers prepared by different processes

Weiwei Qu<sup>1,2,6</sup>, Zehao Chen<sup>3,6</sup>✉, Zhilin Zhang<sup>4</sup>, Xue Li<sup>3</sup>, Fan Yang<sup>2</sup>, Jinlong Wang<sup>3</sup> , Minghui Chen<sup>3</sup> , Shusuo Li<sup>5</sup> and Fuhui Wang<sup>3</sup>

The hot corrosion experiments of René N5 alloy coated with three different NiCrAlY metal bonding layers are carried out, that the layers are prepared by different methods (APS, HVOF and MIP). Compared with bare René N5 alloy samples, the hot corrosion resistance of coated samples is improved. It can be attributed to the small internal stress of the surface oxide layer on the coating sample, which is difficult to spall, reducing the degree of hot corrosion reaction. The hot corrosion resistance of NiCrAlY layers is MIP > HVOF > APS, which is positively positively related to the density of layers, because the influence of element diffusion in the process of hot corrosion is effectively slowed down.

npj Materials Degradation (2024)8:36; <https://doi.org/10.1038/s41529-023-00411-z>

## INTRODUCTION

Gas turbine is widely used as an efficient energy conversion equipment<sup>1</sup>. The most effective way to improve its power and energy conversion efficiency is to increase its inlet temperature<sup>2</sup>. Therefore, it is the focus of researchers to find turbine materials that can withstand high temperatures<sup>3</sup>. Considering the high temperature, harsh chemical environment and complex stress conditions is the turbine faced in its service process<sup>4</sup>. It is difficult to ensure the safety and stable service of turbine components relying on single crystal superalloy<sup>5</sup>. So, the multi-material system, which is provided by nickel-based single crystal superalloy for mechanical properties, thermal barrier coating for temperature isolation, and metal bonding layer for environmental protection and material system stability, is widely used in the turbine blades<sup>6</sup>.

As mentioned above, metal bonded layers often face harsh service conditions, in which the high-temperature hot corrosion behavior caused by molten salt has a significant impact<sup>7</sup>. High-temperature hot corrosion is defined as the rapid oxidation-sulfide failure occurring above 850 °C due to molten Na<sub>2</sub>SO<sub>4</sub> covering the sample surface<sup>8</sup>. Researchers carry out studies on the hot corrosion behavior of metal bonding layers. Rapp et al. are the first to study the hot corrosion behavior of superalloys and obtain the fluxing theoretical model<sup>9</sup>. Gurrappa et al. further analyze the hot corrosion behavior of gas turbine MCrAlY coatings from an elemental point of view<sup>10</sup>. Yuan et al. confirm the corrosion effect of different corrosive media on different elements and demonstrate that Al element is sensitive to Na<sub>2</sub>SO<sub>4</sub><sup>11</sup>. Wang et al. conclude that Co in MCrAlY bonding layer has the effect of improving hot corrosion resistance, while adding Ta would reduce this effect<sup>12</sup>. Mobarra et al. believe that the degradation process of β-NiAl is the main reason for the hot corrosion failure of the MCrAlY coating<sup>13</sup>. Wang et al. conclude that below 800 °C, the addition of Mo is helpful to keep β-NiAl stable, improving the hot corrosion resistance. But with the increase of temperature, this effect gradually deteriorates<sup>14</sup>. Yu et al. also prove that Mo has a negative effect on the oxidation and hot corrosion resistance of the coating when the temperature is above 850 °C<sup>15</sup>. Doolabi et al.

and Chen et al. verify the positive role of Cr in MCrAlY coating in hot corrosion resistance<sup>16,17</sup>.

The role of bonding layer elements in the hot corrosion process is relatively mature. In recent years, studies begin to focus on the different hot corrosion behavior of metal bond layers with different structures by using various preparation methods. Wang et al. study the hot corrosion behavior of MCrAlY coating by MIP, and conclude that MCrAlY coating can effectively improve the hot corrosion resistance of samples through the generation of α-Al<sub>2</sub>O<sub>3</sub><sup>18</sup>. Cai et al. obtain polished, dense and refined radiated surfaces by high-current pulsed electron beam, further improving the hot corrosion resistance of arc ion plating coatings<sup>19</sup>. Sundaresana et al. study the hot corrosion behavior of MCrAlY coating prepared by atmospheric plasma spraying (APS). Compared with other coatings, they find that the hot corrosion resistance of APS coating is poor and the coating is easy to spall<sup>20</sup>. Dong et al. improve the hot corrosion resistance of MCrAlY coating prepared by APS by adding deoxidizer<sup>21</sup>. Jafari et al. find that the MCrAlY coating prepared by HVOF has poor hot corrosion resistance<sup>22</sup>. Hao et al. believe that the direct factor affecting the hot corrosion resistance of HVOF coating is the change of coating structure caused by process parameters. Dense and uniform coating has an excellent hot corrosion resistance<sup>23</sup>. Wang et al. improve the hot corrosion resistance of HVOF coating to a certain extent by means of nano-particles surface<sup>24</sup>. These studies discuss the corrosion mechanism of metal bonding coating and give feasible schemes to improve the hot corrosion resistance of coating. However, there are few studies on the comparison of hot corrosion behavior of MCrAlY coatings prepared by different methods. The research on the hot corrosion behavior of different coating-substrate interface and the distribution of elements in different coatings during the hot corrosion process are also insufficient. It is of great significance to carry out relevant research for the purpose of develop metal bonding layers with good bonding ability and hot corrosion resistance<sup>25</sup>.

In this study, three kinds of coatings prepared in different ways (APS, MIP, HVOF) are tested for hot corrosion. At the same time, the uncoated samples are used as the control group to analyze

<sup>1</sup>Shenyang Aeroengine Research Institute, Aero Engine Corporation of China, Shenyang 110015, China. <sup>2</sup>School of Materials Science and Engineering, Beihang University, No. 37 Xueyuan Road, Beijing 100191, China. <sup>3</sup>Shenyang National Laboratory for Materials Science, Northeastern University, Shenyang 110819, China. <sup>4</sup>Institute of Systems Engineering, China Academy of Engineering Physics, P.O.Box 919-412, Mianyang 621900 Sichuan, China. <sup>5</sup>Institute of Aero Engine Research, Beihang University, No. 37 Xueyuan Road, Beijing 100191, China. <sup>6</sup>These authors contributed equally: Weiwei Qu, Zehao Chen. ✉email: [chenzehao@mail.neu.edu.cn](mailto:chenzehao@mail.neu.edu.cn); [mhchen@mail.neu.edu.cn](mailto:mhchen@mail.neu.edu.cn)

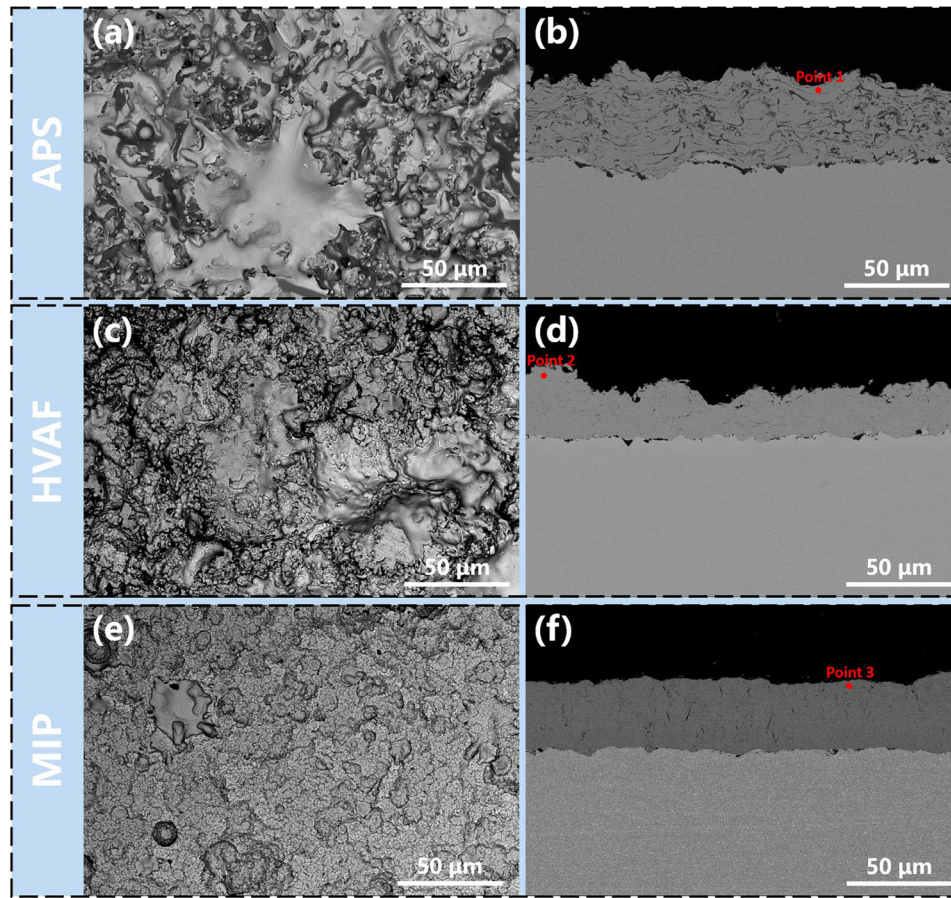


**Fig. 1** The surface and cross-section morphology of NiCrAlY coatings fabricated via three methods on René N5 alloy. **a** Surface of APS coating, **b** cross-section morphology of APS coating, **c** surface of HVAF coating, **d** cross-section of HVAF coating, **e** surface of MIP coating, **f** cross-section morphology of MIP coating.

the hot corrosion resistance of the coating. The hot corrosion salt is 75%  $\text{Na}_2\text{SO}_4$  + 25% NaCl, and the experimental temperature is set at 900 °C. Furthermore, the hot corrosion resistance of each coating and the mechanism are described in combination with the stress analysis of the coating-substrate interface, the chemical potential distribution of elements inside the coating and the hot corrosion reaction thermodynamics in each stage of the hot corrosion.

## RESULTS

### Microstructure of the coatings

NiCrAlY coatings are deposited on the surface of René N5 single crystal superalloy by APS, HVAF and MIP. The surface and cross-section microstructure of three coatings are shown in Fig. 1. In addition, the porosity, thickness and composition of three coatings are showed in Supplementary Table 2 and Supplementary Table 3. Due to the different principle of three preparation methods, the microstructure of surface and cross-section morphology is significantly different. The surfaces of APS coating and HVAF coating (Fig. 1a, c) present typical thermal spraying morphology, which can be observed that the droplets with large size are bombarded with larger roughness. The surface porosity of APS coating is about 14.286% (measured by Image J software), while that of HVAF coating is about 10.069%. The cross-section of APS coating (Fig. 1b) shows obvious lamellar structure, and a large number of strips  $\text{Al}_2\text{O}_3$  oxide slag inclusions are included between

layers. The average thickness of the coating is about 80  $\mu\text{m}$ , and there are many impurity phases near the coating/substrate interface. The cross-section of HVAF coating (Fig. 1d) presents a layered structure with fewer impurity phases. The average thickness of the coating is about 50  $\mu\text{m}$ , and there are a few amounts of large size impurity phases near the coating/substrate interface. The surface and cross-section of MIP coating (Fig. 1e, f) show the characteristic of physical vapor deposition. Obvious finer particle bombardment morphology and smaller roughness can be observed. The surface porosity is about 3.750%, and the average thickness of the coating is about 70  $\mu\text{m}$ . The existence of few internal impurity phases with a vertical strip shape indicates that the coating has a vertical dendrite structure. The size and quantity of impurity phases near the coating/substrate interface are the smallest compared with the other two coatings.

### Thickness of the hot corrosion layer

René N5 alloy and three coatings are corroded by high-temperature molten salt at 900 °C for up to 200 h. Samples corroded for 5 h, 20 h, 50 h, 100 h and 200 h are selected to measure the change of the thickness of the reaction layer on the cross-section as shown in Fig. 2. Reaction layer is the area influenced by hot corrosion reaction of alloy or coatings, which is clearly different from substrate in microstructure. The change in thickness of reaction layer is the sum of the thickness change of the oxide layer on the sample surface and the subsurface corrosion affected zone (where many internal corrosion products

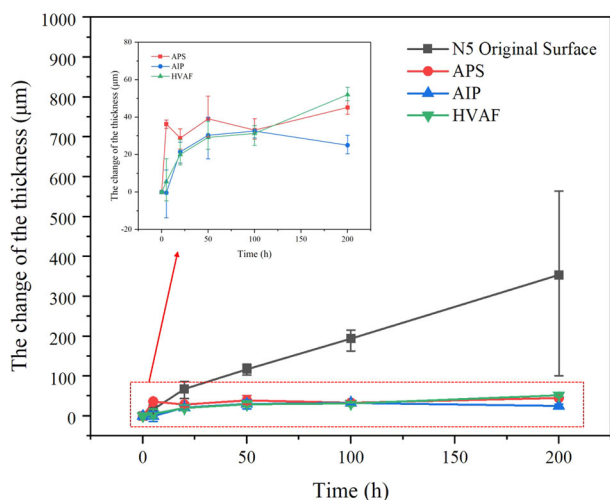


**Fig. 2** The diffusion layer thickness of René N5 alloys with four surface condition corroded by molten salt in the air at 900 °C. The error bar is standard deviation.

are precipitated). It can reflect the difference of resistance of René N5 with four different surface states to the permeation of molten salt hot corrosion. Compared with the original surface states of René N5 alloy (whose average thickness change rate is  $1.59 \mu\text{m h}^{-1}$ ), the NiCrAlY coating can effectively reduce the thickening rate of the reaction layer (whose average thickness change rate is less than  $0.25 \mu\text{m h}^{-1}$ ), which means it significantly improve the hot corrosion resistance. The thickness of APS coating reaction layer increases rapidly during the first 5 h of hot corrosion (about  $7.26 \mu\text{m h}^{-1}$ ), which may be due to the large porosity of the surface and the internal channel for molten salt infiltration formed by internal defects. In the next 5 h–200 h of hot corrosion process, the thickness curve of APS coating presents a trend of wavy line variation, but the average thickness is basically maintained in the range of 100–120  $\mu\text{m}$ , which indicates that the coating can effectively prevent the hot corrosion reaction of molten salt from extending to the interior of alloy matrix in spite of molten salt can penetrate into APS coating quickly in the early stage. The thickness curves of HVAF coating and MIP coating show almost the same trend in the first 100 h of hot corrosion with a parabolic shape. The average thickness increases rapidly during the first 20 h of hot corrosion (the average thickness change rate of MIP coating is  $1.072 \mu\text{m h}^{-1}$  while that of HVAF coating is  $1.001 \mu\text{m h}^{-1}$ ), then the increase rate decreases gradually during 20 h–100 h of hot corrosion. However, it can be observed that the change of thickness of two coatings shows differentiation after 100 h of hot corrosion, in which MIP coating shows a decreasing trend while HVAF coating shows an increasing trend.

### The surface morphology and products after hot corrosion

The surface morphologies of René N5 alloy and three coatings are observed after 200 h hot corrosion and the corrosion products are characterized. The results are shown in Fig. 3. It can be observed that the number and size of cracks and spalling on the surface of three coatings decrease significantly after 200 h of hot corrosion, compared with a large number of cracks and spalling of larger sizes (greater than 400  $\mu\text{m}$ ) on the original surface of René N5 alloy. According to the X-ray diffraction (XRD) patterns of each surface (Fig. 3e), NiO phase,  $\text{Al}_2\text{O}_3$  phase and little spinel structural phase (including  $(\text{Ni}, \text{Co})\text{Cr}_2\text{O}_4$  and  $(\text{Ni}, \text{Co})\text{Al}_2\text{O}_4$ ) mainly exist on the surface of René N5 alloy, while  $\text{Ni}_x\text{Al}$  phase ( $x \geq 1$ ),  $(\text{Al}_y\text{Cr})_2\text{O}_3$  phase, (mixture of  $\text{Al}_2\text{O}_3$ ,  $\text{Cr}_2\text{O}_3$ ), spinel structural phase and

$\text{NaY}[(\text{Mo}, \text{W})\text{O}_4]_2$  structural phase mainly exist on the surface of three processes. In addition, there are certain differences in the peak intensity of corrosion products on different coating surfaces. The  $\text{Ni}_x\text{Al}$  phase is the structural phase of the coating or substrate, indicating that the thickness of oxide layer on the coating sample surface is less than the XRD detection depth of 5–20  $\mu\text{m}$ .

### Microstructure of cross-section after hot corrosion

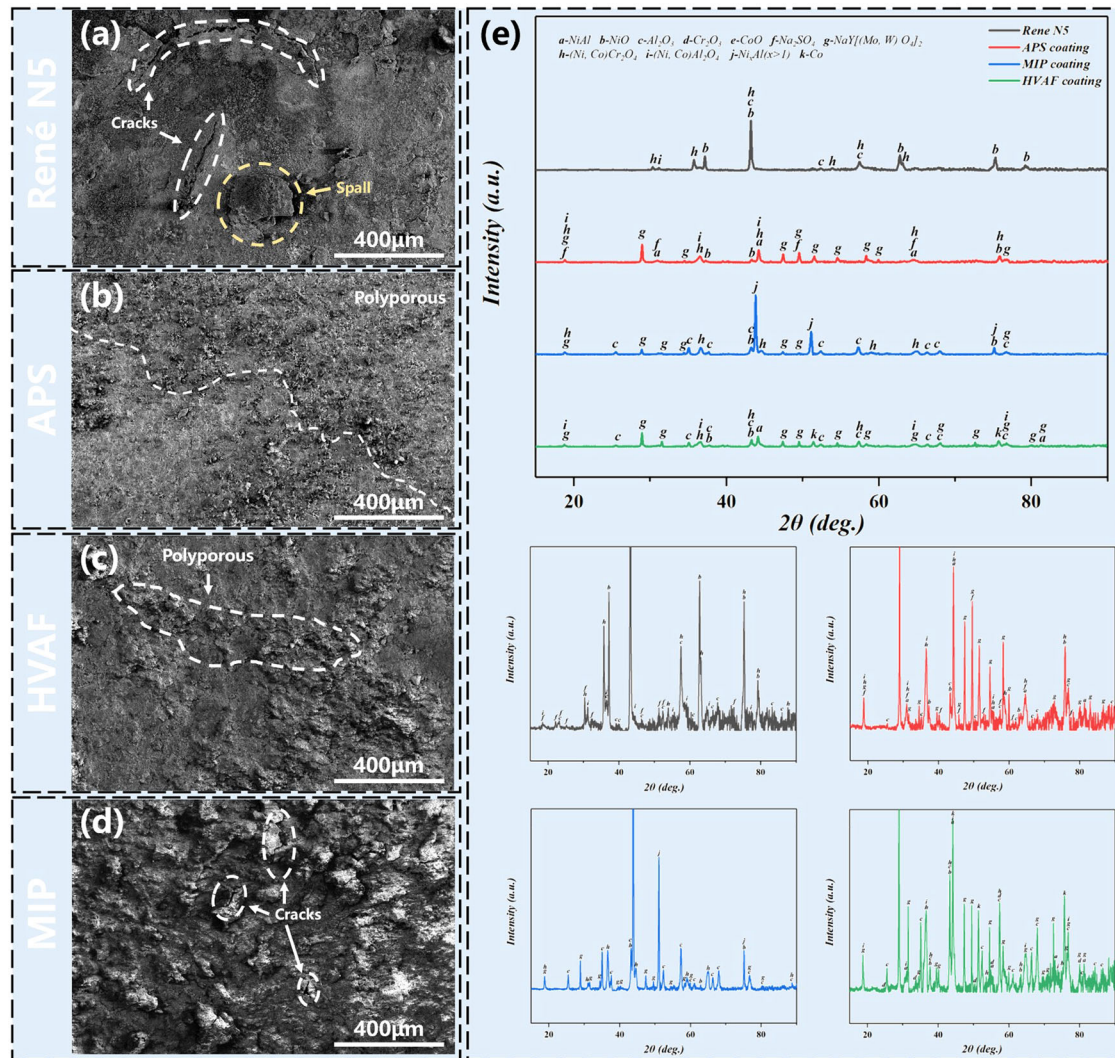
Fig. 4 shows the BSE images of the cross-sections of René N5 alloy corroded by molten salt at 900 °C for 20 h, 50 h, 100 h and 200 h. It can be seen that there is a significant impact on the cross-section of the alloy: A large number of corrosion products are generated on the surface and inside of the alloy, resulting in serious degradation of the subsurface structure and in reduction of the effective bearing area of the cross-section. The phenomena are intensified with the continuous hot corrosion. The main components of the oxide layer are outer  $\text{Cr}_2\text{O}_3$  layer and inner  $\text{Al}_2\text{O}_3$  layer. At 200 h of hot corrosion (Fig. 4d), some large size cracks appear between  $\text{Cr}_2\text{O}_3$  layer and  $\text{Al}_2\text{O}_3$  layer with serious spalling. There is an obvious interface between the reaction layer and the substrate, and a large amount of sulfide phase ( $\text{Cr}_x\text{S}$ ) precipitates above the interface. In general, René N5 alloy exhibits catastrophic morphology after hot corrosion under given experimental conditions.

Fig. 5 shows the BSE images of the cross-sections of APS, HVAF and MIP coatings at 900 °C for 5 h, 20 h, 50 h, 100 h and 200 h. It can be seen that compared with original surface of René N5 alloy, three coatings all show better cross-sections morphology after hot corrosion, in which thin continuous dense oxide layer is formed on the surface with less spalling and no obvious cracks. Although three coatings control the reaction layer affected by hot corrosion within a certain range, there are obvious differences in the cross-section microstructure evolution of different coatings.

Fig. 5a, d, g, j, m show that a continuous and dense  $\text{Al}_2\text{O}_3$  layer is rapidly formed on the APS coating surface under the influence of hot corrosion, accompanied by the generation of little spinel phase ( $\text{NiCr}_2\text{O}_4$ , etc.). With the continuous aggregation of Cr elements towards the oxide layer/coating interface, a large amount of  $\text{Cr}_2\text{O}_3$  is subsequently generated on the coating surface. This results in obvious stratification of the oxide layer, where  $\text{Cr}_2\text{O}_3$  tends to occupy the outermost layer and  $\text{Al}_2\text{O}_3$  tends to occupy the inner layer. At the same time, the dispersion oxide phase (mainly  $\text{Al}_2\text{O}_3$ ) inside the APS coating grows and connects with each other, and little small point-like Cr-rich phases (mainly Cr,  $\text{Cr}_2\text{O}_3$ ,  $\text{Cr}_x\text{S}$ , etc.) attach to the interface of the oxide slag phase to nucleate and grow. In addition, many large geometric point-like Cr-rich phases (mainly  $\text{Cr}_x\text{S}$  phase) are precipitated in the substrate depleted zone below the coating.

As shown in Fig. 5b, e, h, k, n, the oxide layer with  $\text{Al}_2\text{O}_3$  as the main component (in which  $\text{Cr}_2\text{O}_3$  atom accounts for about 7%) is formed quickly on the surface of HVAF coating at first, while a large amount of internal oxide phase (mainly  $\text{Al}_2\text{O}_3$ ) is precipitated at the interior of coating and the coating/substrate interface. With the continuous hot corrosion, the thickness of the oxide layer on the coating surface increases and the composition of the oxide layer becomes complex. Many bright white Ta-rich oxide phases are enriched at the oxide layer/coating interface. At the same time, the number of oxides at the interior of coating and the coating/substrate interface increases, showing a tendency to grow and combine with Cr-rich small precipitation. Part of the substrate below the coating/substrate interface is depleted with the  $\gamma/\gamma'$  phase structure disappeared, where geometrically point-like Al-rich and Cr-rich sulfide phases are precipitated and dispersed.

MIP coating shows different corrosion behavior characteristics and better microstructure stability in the same experiment environment. As shown in Fig. 5c, f, i, l, o,  $\text{Al}_2\text{O}_3$  occupies a high proportion in the oxide layer and the size of oxide layer is uniform.



**Fig. 3** The surface morphology. **a** René N5 alloys corroded by molten salt in the air at 900 °C for 200 h, **b** APS coating surface corroded by molten salt in the air at 900 °C for 200 h, **c** HVAF coating surface corroded by molten salt in the air at 900 °C for 200 h, **d** MIP coating surface corroded by molten salt in the air at 900 °C for 200 h, **e** XRD patterns.

Many Al-rich phases (partly  $\text{Al}_2\text{O}_3$  and partly oxygen-poor phase) are precipitated inside the coating. In addition, the precipitated phase presents small speckled distribution, and only a small amount of  $\text{Al}_2\text{O}_3$  shows the trend of growth and connection. A large number of continuously distributed Al-rich phases with large size is precipitated at part of the coating/matrix interface, while almost no precipitated phases are generated at other part of the coating/matrix interface, which forming a sharp contrast as shown in Fig. 5l, o. The substrate depleted zone is still formed under the coating/ substrate interface. However, the thickness of the substrate depleted zone is thinner than that of the other two coatings. Fewer and smaller geometric point Al-rich and Cr-rich phases are precipitated in part of the zone, and their distribution seems to be positively correlated with the existence of continuous Al-rich phases at the interface.

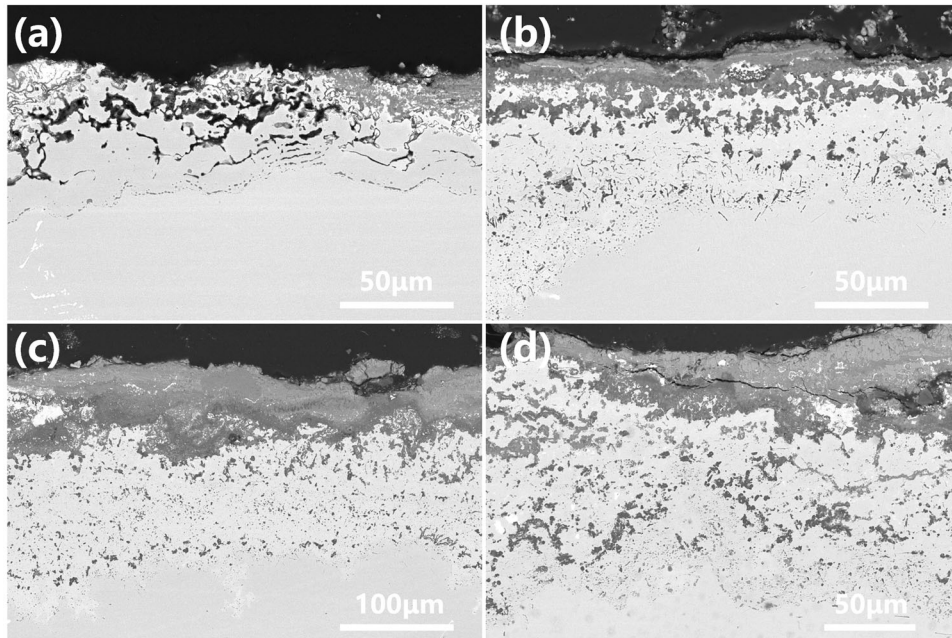
Fig. 6 shows the distribution of cross-section elements of the three coatings after 200 h hot corrosion. It can be obviously observed that most O element is fixed by Al element, which is mainly distributed on the surface and inside the coating, corresponding to the position of corrosion products. Cr element is mainly concentrated in the inner position of the coating, which is less consistent with the O element. In the element distribution

diagram of three coatings, the MIP process coating fixes more O and Al elements on the surface, but less uneven enrichment and distribution of S and Cr elements inside the coating, which makes the distribution of Ni elements more continuous. This indicates that MIP coating has better microstructure stability and hot corrosion resistance in 900 °C under the attack of molten salt.

## DISCUSSION

According to the experimental results, compared with bare alloy, the hot corrosion resistance of samples coated MCrAlY is significantly improved. There are two main reasons for this phenomenon. One is the degree of chemical reaction caused by hot corrosion, and the other is the stability of the surface reaction layer.

The essence of hot corrosion is that molten salt destroys the integrity of the oxide layer on the surface of the alloy, making the oxide layer loses its protective effect and the oxidation reaction on the surface of the alloy can continue, so as to continuously consume the components of the alloy and accelerate the degradation and failure of the surface and near surface of the alloy. Especially for the early stage of hot corrosion reaction, the formation of stable and dense oxide layer affects the subsequent

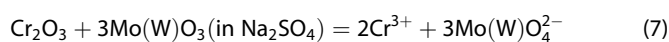
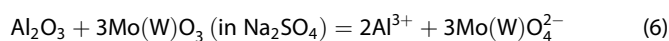
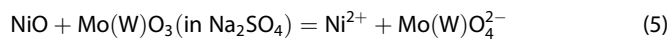


**Fig. 4** The BSE cross-section morphology of René N5 alloys without coating corroded by molten salt in the air at 900 °C. **a** Corroded by molten salt for 20 h, **b** corroded by molten salt for 50 h, **c** corroded by molten salt for 100 h, **d** Corroded by molten salt for 200 h.

hot corrosion. For hot corrosion of superalloys, the following reactions occur:



Under normal circumstances, the surface oxide layer composed of NiO, Al<sub>2</sub>O<sub>3</sub> and Cr<sub>2</sub>O<sub>3</sub> can isolate molten salt and prevent oxidation to a certain extent. Although it will gradually dissolve in molten salt with the progress of hot corrosion, it can obviously prevent molten salt in the initial period of hot corrosion. However, for the second-generation single crystal superalloy René N5 adopted in this study, the mechanical properties strengthen element Mo and W contained in it will reduce the protective effect of the oxide layer on the surface, through the following reaction:



Considered that the standard Gibbs free energy of each oxidation reaction presents: NiO > MoO<sub>3</sub> > Cr<sub>2</sub>O<sub>3</sub> > Al<sub>2</sub>O<sub>3</sub>, as shown in Fig. 7. When hot corrosion occurs, protective Al<sub>2</sub>O<sub>3</sub> and Cr<sub>2</sub>O<sub>3</sub> preferentially form on the sample surface. As the reaction continues, internal Mo element diffuses to the sample surface, forming MoO<sub>3</sub>, and the reaction as shown in Eqs. (5), (6), and (7) occur, destroying the integrity of the surface oxide layer and generating crack sources, as shown in schematic Fig. 8.

For the coating samples, the main component of the coating is NiCrAlY. This means that Mo, W and other elements are difficult to

have a significant impact on the process of hot corrosion at the initial stage (the formation stage of the surface oxide layer). Therefore, although the phenomenon of fluxing still occurs, the surface reaction layers remain relatively intact, and crack sources will not easily generate.

According to the experimental results, it can be found that compared with the coated samples, the bare alloy has an obvious surface spallation phenomenon. The hot corrosion reaction process affected by the above elements can effectively explain the crack origin of the spallation surface layer of the bare alloy. During the thermal corrosion process, the difference in the stress state of the oxide layer between the coated sample and the bare alloy leads to the difference in the spalling behavior, as explained below<sup>26,27</sup>.

In this study, Abaqus software is used to analyze the stress of the surface layer. Two models are designed: oxide layer-matrix model and oxide layer-bonding layer-matrix model. The specific parameters are displayed in Supplementary Table 4 and Supplementary Table 5. Fig. 9 shows the stress state of the oxide layers on the surface of different samples in the presence or absence of a bonding layer. It can be found that when the bonding layer exists as shown in Fig. 9a, the stress distribution inside the surface oxide layer is uniform, and the value is small. However, when the oxide layer directly exists on the substrate surface as shown in Fig. 9b, the local stress of the oxide layer is large, and the internal stress distribution is not uniform, that is, the stress at the center of the oxide layer is larger. The result of this phenomenon is that when hot corrosion occurs, the oxide layer on the bare alloy surface tends to bulge or crack under the action of chemical reaction and interaction temperature compared with the sample with bonding layer. It can be attributed to the matching effect of thermal expansion of bonding layer. The thermal expansion coefficient of nickel-based superalloys is generally  $\sim 1.75 \times 10^{-5} \text{ K}^{-1}$ , and the thermal expansion coefficient of the outer oxide (take alumina as an example) is generally  $\sim 0.90 \times 10^{-5} \text{ K}^{-1}$ <sup>28,29</sup>. There is an obvious mismatch between the oxide layers and the matrix. For the MCrAlY bonding layers, based on its intrinsic properties and internal porous

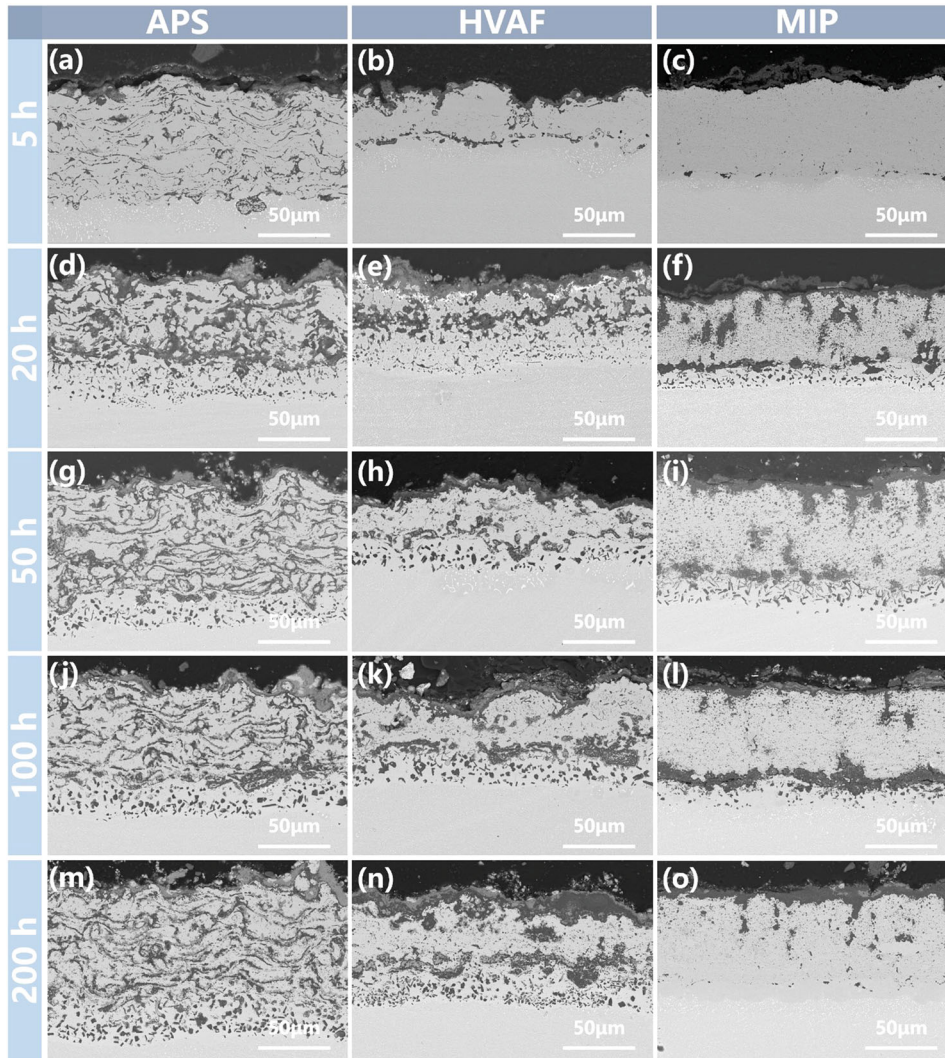


**Fig. 5** The BSE cross-section morphology of three different preparation methods of coatings corroded at 900 °C. **a** APS coating corroded after 5 h, **d** APS coating corroded after 20 h, **g** APS coating corroded after 50 h, **j** APS coating corroded after 100 h, **m** APS coating corroded after 200 h, **b** HVOF coating corroded after 5 h, **e** HVOF coating corroded after 20 h, **h** HVOF coating corroded after 50 h, **k** HVOF coating corroded after 100 h, **n** HVOF coating corroded after 200 h, **c** MIP coating corroded after 5 h, **f** MIP coating corroded after 20 h, **i** MIP coating corroded after 50 h, **l** MIP coating corroded after 100 h, **o** MIP coating corroded after 200 h.

microstructure, its thermal expansion coefficient is usually  $\sim 1.20 \times 10^{-5} \text{ K}^{-1}$ <sup>30</sup>. This well weakens the stress difference between the substrate and the surface oxide layer, and decreases the internal stress of the surface oxide layer, thus reducing the possibility of surface layer spalling.

In a word, for samples with MCrAlY coating, the presence of coating can effectively weaken the chemical reaction degree of hot corrosion and ensure the formation of stable oxide layer. Meanwhile, coating can reduce the internal stress of surface layer caused by the thermal mismatch between surface oxide layer and matrix. Therefore, the presence of MCrAlY coating can effectively delay the surface spallation and reduce the influence of hot corrosion on samples.

Of the three coating preparation methods used in this study, APS is the most commonly used in industry. In order to ensure high strain tolerance, APS coatings have high porosity and lamellar structure, which means that the hot corrosion resistance of APS coatings is hard to be outstanding. Fig. 10a, d, g show the section morphology, element distribution and chemical potential trend of APS coating samples at 5 h, 100 h and 200 h with the

progress of hot corrosion. It can be seen that at 5 h of hot corrosion as shown in Fig. 10a, diffusion barrier formed by composite oxide layer appears on the surface of the sample; oxides are generated inside the coating; and diffusion barrier of Cr is formed at the interface between coating and matrix. However, from the perspective of chemical potential, Al element diffuses from the matrix to the coating direction. When the reaction lasts for 100 h as shown in Fig. 10d, the oxide layer on the surface still exists but is not dense. In addition, serious internal oxidation occurs on the coating, and the inter-diffusion zone (IDZ) at the interface between the matrix and the coating is formed, connecting the inner regions of the coating. From the perspective of chemical potential, the coating loses the effect of elements diffusion resistance. When the hot corrosion continues to 200 h as shown in Fig. 10g, the thickness of the reaction layer of the sample increases. The surface oxidation layer is obviously spalling; the oxidation inside the coating becomes more serious; and the IDZ becomes irregular. From the perspective of chemical potential, APS coating basically loses the ability to prevent the

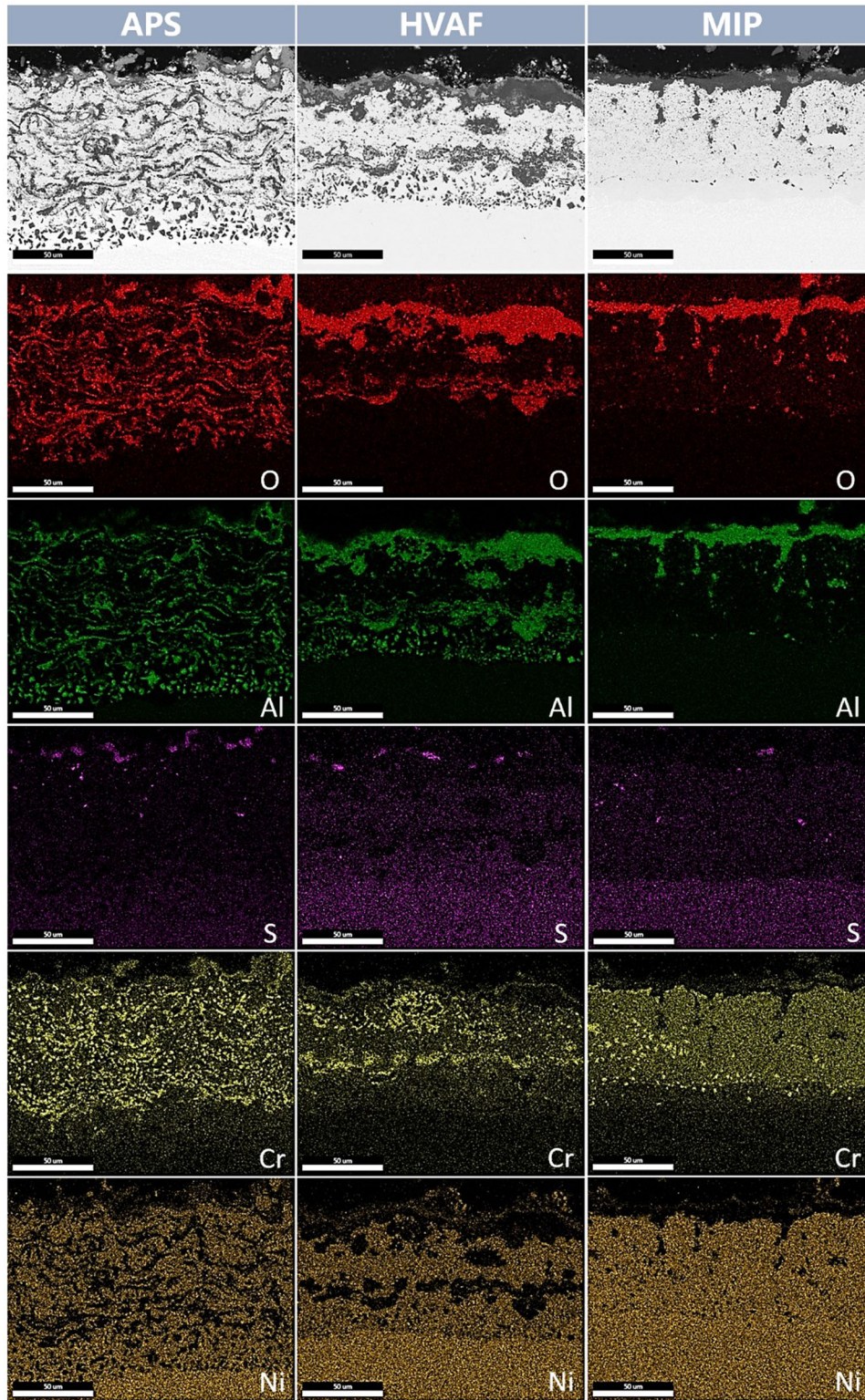


**Fig. 6** The EDS elements distribution of three coatings corroded by molten salt in the air at 900 °C for 200 h. From left to right, the APS, HVOF, MIP samples and the distribution of O, Al, S, Cr, Ni elements are shown.

diffusion of elements, that is, it does not have the ability to further resist hot corrosion.

Compared with the coating prepared by APS method, MIP coating has a denser structure, but there are still some pores in the interface between matrix and coating due to the high

temperature difference of preparation. Fig. 10b, e, h show the variation trend of the section morphology, element distribution and chemical potential of MIP coating samples at 5 h, 100 h and 200 h with the progress of hot corrosion. It can be seen that at 5 h of hot corrosion as shown in Fig. 10b, a layer consisting mainly of

$\text{Al}_2\text{O}_3$  is formed on the surface of the sample. At the same time, some oxides are formed at the interface between matrix and coating, but the oxidation behavior in the coating is not obvious. Further analysis shows that the element diffusion barrier is formed on the surface of the sample and the interface between substrate and coating, which delays the initial reaction of hot corrosion. At 100 h, the degree of hot corrosion obviously deepens as shown in Fig. 10e. Although the oxide layer on the surface of the sample remains intact, oxidation within the coating inevitably occurs. Compared with APS coating samples, the oxidation in MIP coating is not serious, and IDZ is formed in the interface between matrix and coating, and the effect of diffusion barrier is maintained. The thickness of the reaction layer does not change obviously when the hot corrosion continues to 200 h as shown in Fig. 10h. With

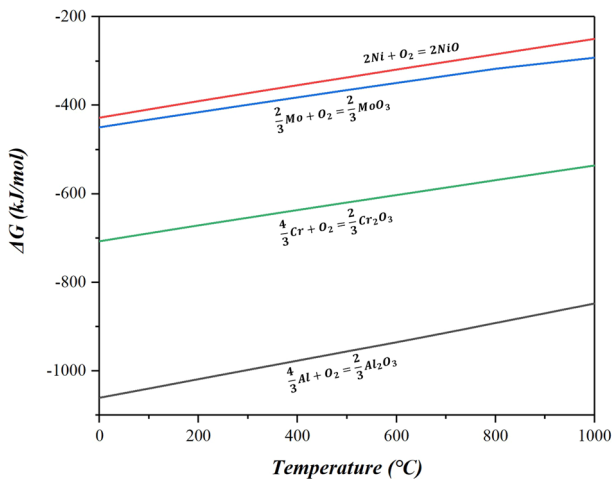


**Fig. 7** The standard Gibbs free energy of each oxidation reaction. Gibbs free energy curve of Ni, Mo, Cr, Al oxidation reaction.

the progress of hot corrosion, the changes of samples include two points: 1. The thickness of oxide layer on the surface increases; 2. The area of IDZ increases. From the perspective of chemical potential, both of them can be regarded as elemental diffusion barriers to improve the hot corrosion resistance of samples. However, it is worth noting that the proportion of MCrAlY coating that provides element support for the stable existence of the oxide layer and IDZ gradually decreases, which means that the power of coating for the hot corrosion resistance of the sample gradually declines. This is why MIP samples has a decreasing trend of hot corrosion resistance.

As a coating preparation method with different layer forming methods, HVAF has a good coating-matrix bonding force, and its coating density is higher than the other two preparation methods. Figs. 10c, f, i show the variation trend of the section morphology, element distribution and chemical potential of HVAF coating samples at 5 h, 100 h and 200 h with the progress of hot corrosion. It can be found that reaction products are generated on the surface of the coating and the interface between the coating and the matrix when the hot corrosion lasts for 5 h as shown in Fig. 10c. An oxide layer mainly composed of  $\text{Al}_2\text{O}_3$  is formed on the surface of the sample, forming a diffusion barrier of corrosive elements. There is basically no reaction inside the coating; and the chemical potential between the coating and the matrix is similar; the elements mutual diffusion trend is not shown. When the hot corrosion lasts for 100 h, the reaction layer region of the sample remains within the coating range, and only the interdiffusion region about  $10\ \mu\text{m}$  appears at the interface between coating and matrix as shown in Fig. 10f. The surface oxidation layer of the sample remains intact, and some internal oxidation occurs in the coating. It is noteworthy that a continuous and dense oxide layer appear at the coating-matrix interface, which becomes the diffusion barrier of Al, Cr, O and other elements, balancing the chemical potential of elements on both sides, and greatly reducing the adverse effect of internal corrosion and oxidation on the sample. When

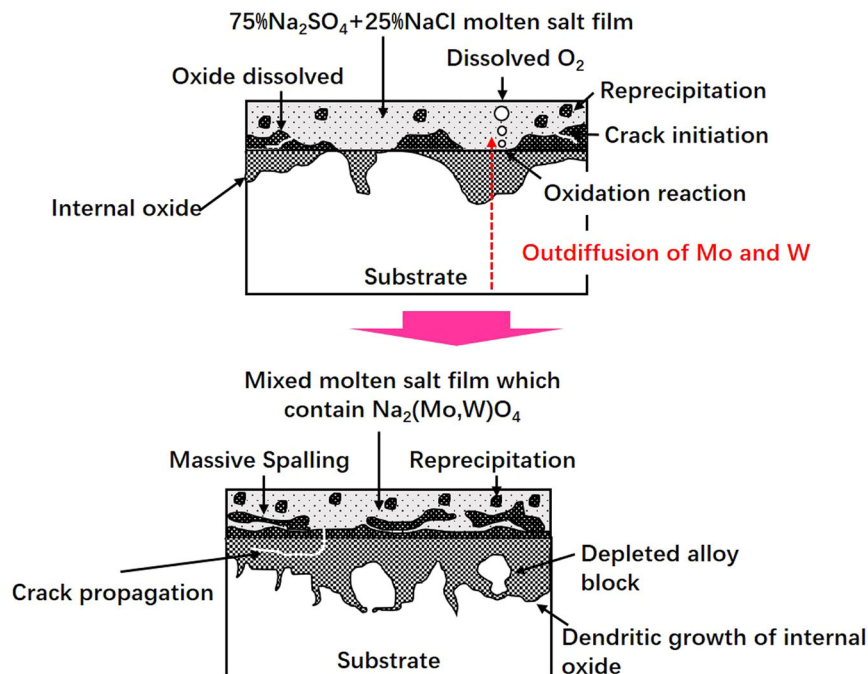


**Fig. 8** Schematic diagram of catastrophic hot corrosion occurring. The difference between conventional hot corrosion and high Mo alloy hot corrosion process.



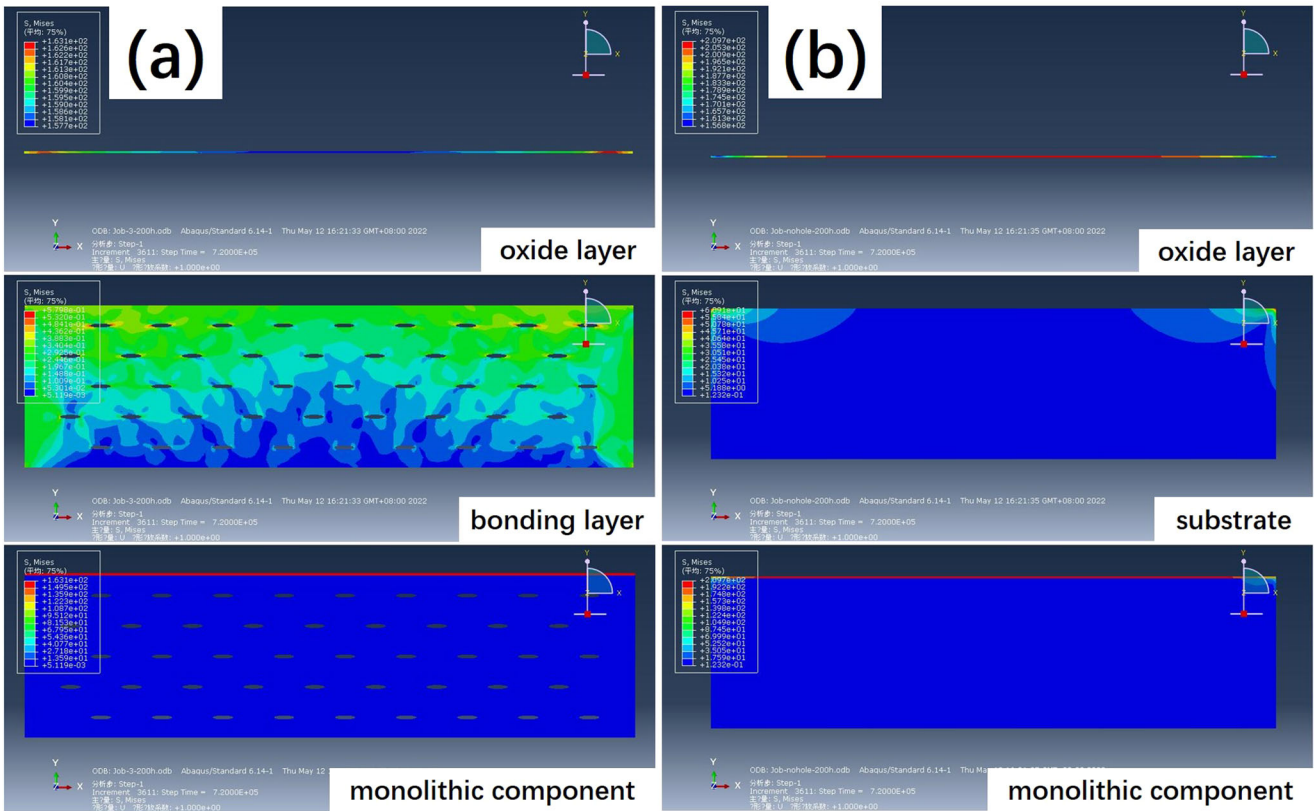


**Fig. 9** Diagram of stress distribution in the samples. **a** Sample with NiCrAlY bonding layer; **b** sample without NiCrAlY bonding layer (bare René-N5 alloy).

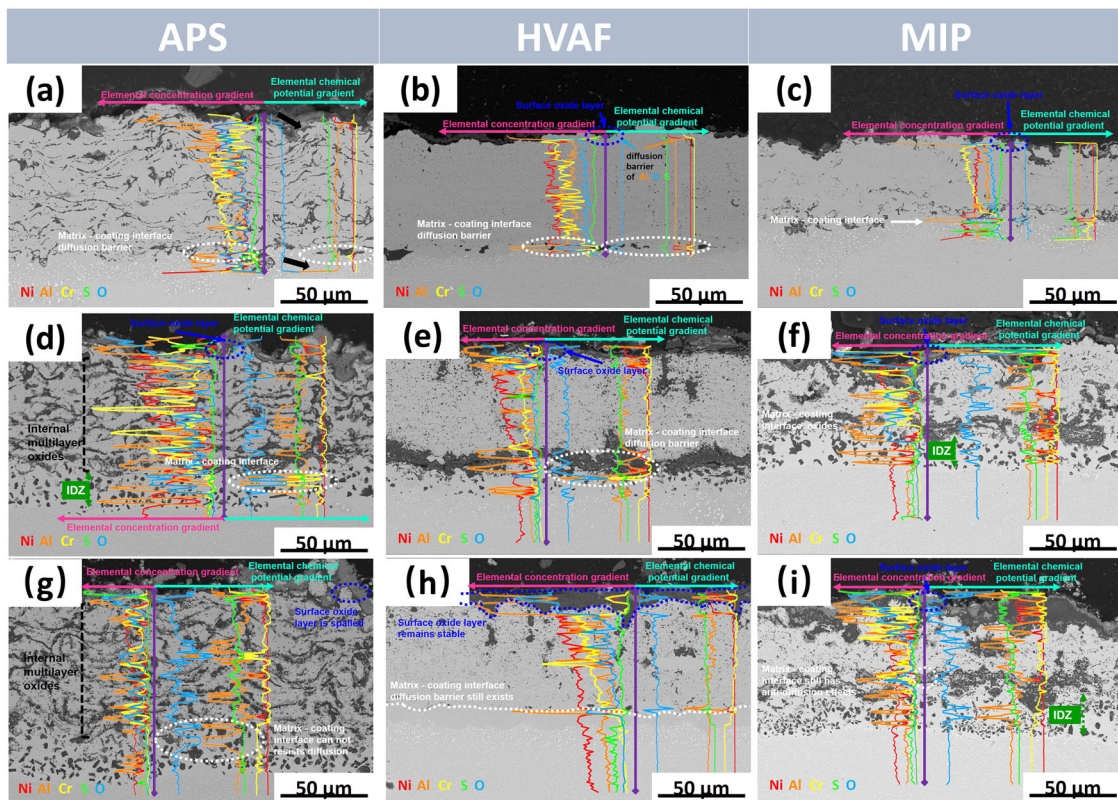


**Fig. 10** The section morphology, element distribution and chemical potential trend (Thermal-calc). **a** APS coating corroded at 5 h, **d** APS coating corroded at 100 h, **g** APS coating corroded at 200 h; **b** HVAF coating corroded at 5 h, **e** HVAF coating corroded at 100 h, **h** HVAF coating corroded at 200 h; **c** MIP coating corroded at 5 h, **f** MIP coating corroded at 100 h, **i** MIP coating corroded at 200 h.

the hot corrosion continues until 200 h, the oxide layer on the surface of the sample is still stable and compact, so the oxidation in the coating is not serious as shown in Fig. 10i. With the continuous hot corrosion, the inner oxide layer disappears at the interface between coating and matrix, and there is chemical potential fluctuation at the interface. However, there is no chemical potential difference between the main elements on both sides of the interface, so there is no obvious element diffusion trend. The dense oxide layer on the surface is sufficient to prevent the further aggravation of hot corrosion.

Comprehensive analysis of the hot corrosion resistance of the three coatings shows that MIP is better than HVOF, and HVOF is better than APS. The most intuitive reason for this result is the difference in porosity of the three coatings. The coating of MIP is the densest, resulting in the oxidation layer formed on the surface remaining intact, and reducing the corrosive element channels in the coating, so its hot corrosion is inhibited. APS coating has high porosity, which means that external corrosive elements and internal matrix metal elements are easy to diffuse. It intensifies the internal reaction of the coating, resulting in the loss of the protective effect of the coating and the inability to prevent the continuous occurrence of thermal corrosion. For HVOF coating, although the coating is relatively dense and the oxide layer on the surface is stable, there are diffusion channels at the interface between the coating and the matrix, which is easy to cause the degradation of the coating and reduce the hot corrosion resistance of the sample.

In conclusion, through the analysis of the microstructure characteristics of the NiCrAlY layer and the subsequent hot corrosion experiment, the following conclusions can be drawn:

1. NiCrAlY coating can greatly improve the hot corrosion resistance of the sample, and the coating does not spall in the process of hot corrosion basically.
2. The presence of coating can greatly reduce the internal stress of the oxide layer on the surface, and then reduce the penetration effect of molten salt.
3. The hot corrosion resistance of NiCrAlY coating is MIP > HVOF > APS.
4. The hot corrosion resistance of NiCrAlY coating mainly depends on the density of coating and the ability of element diffusion caused by the stability of oxide layer on the surface. Especially the O and S elements on the outside and the Al and Cr elements on the inside.

## METHODS

### Preparation of materials

The nominal composition (wt%) of René N5 alloy and NiCrAlY coating used in this experiment are showed in Supplementary Table 1.

René N5 single crystal superalloy rods are prepared by liquid metal cooling (LMC) process. The pouring temperature is 1550 °C and the withdraw rate is 6 mm min<sup>-1</sup>. The seed technique with (001)-direction is used to ensure the alloy growing to single crystal. The alloy rods are successively received a solution heat treatment at 1310 °C, 1315 °C and 1320 °C for 2 h followed by air-cooled (AC). Subsequently, the rods are subjected to an aging heat treatment of 1120 °C/4 h/AC and 900 °C/12 h/AC. The hot corrosion specimens with a dimension of  $\varnothing 10 \times 3$  mm are cut by electro-spark wire-electrode cutting and machined cylindrical sides by a lathe. The surfaces of these specimens are prepared by grinding to #1000 emery papers and cleaned subsequently in alcohol to remove dirt.

Atmospheric plasma spraying (APS) process, high velocity air fuel (HVOF) process and multi-arc ion plating (MIP) process are used to deposit NiCrAlY coating of a certain thickness on René N5 specimens, respectively. APS process parameters are as follows:

argon gas flow rate is 40 L min<sup>-1</sup>; hydrogen flow rate is 8 L min<sup>-1</sup>; current is 600 A; power is 35 kW; powder feeder rotary speed is 30%; carrier gas flow rate is 5 L min<sup>-1</sup>. HVOF process parameters are as follows: compressed air pressure is 120 psi; propane pressure is 100 psi; nitrogen pressure is 40 psi; hydrogen pressure is 20 psi; powder feeder rotary speed is 5%; carrier gas flow rate is 30 L min<sup>-1</sup>. MIP process parameters are as follows: arc current is 130 A; bias voltage is 30 V; time is 2 h base pressure is  $5 \times 10^{-3}$  Pa; argon flow is 200 sccm; air pressure is 0.8 Pa.

In view of the morphology characteristics and composition distribution of the coating are easily affected by preparation process, so the preparation processes adopted in this study are the standardized preparation process, that is, a common industrial coating preparation method, to ensure the accuracy and value of the study.

### Hot corrosion testing

All the hot corrosion tests in this experiment are carried out in a box furnace. The original René N5 alloy and three coatings prepared by different processes are sprayed with saturated aqueous solution of 75 wt.% Na<sub>2</sub>SO<sub>4</sub> + 25 wt.% NaCl before drying in a dryer. After drying, the specimens are weighed by a balance to ensure that 0.3–0.5 mg cm<sup>-2</sup> salt is obtained on sprayed surface of each specimen. Each specimen is then put into a crucible, then crucibles are placed into a box furnace to proceed the hot corrosion at 900 °C in atmospheric environment with a cycle period of 5 h. After each cycle, the specimens are taken out and cooled to room temperature. When the experiment is carried out for 5 h, 20 h, 50 h, 100 h and 200 h, the specimens are taken out for characterization.

### Analyzing methods

Analytical balance with minimum sensitivity to 0.01 mg is used to weigh and control the amount of salt applied after each cycle. Scanning electron microscopy with SE (only surface structure) and BSE detectors equipped with an energy dispersive spectroscopy and XRD are used to observe the surface and cross-section morphology, characterize the distribution of elements and identify the corrosion products. Thermal-calc software is used to analyze the diffusion process of elements during the hot corrosion process of specimens.

### DATA AVAILABILITY

The raw/processed data required to reproduce these findings cannot be shared at this time as the data also forms part of an ongoing study.

Received: 17 May 2023; Accepted: 30 October 2023;

Published online: 09 April 2024

## REFERENCES

1. Soares, C. *Gas Turbines: A Handbook of Air, Land, and Sea Applications* (Butterworth-Heinemann, 2008).
2. Sharma, A., Sadeghi, F. & Sharma, A. Experimental investigation of fretting wear of coated spring clip and inlet ring in land-based gas turbines at elevated temperature. *Wear* **446–447**, 203200 (2020).
3. Salwan, G. K., Subbarao, R. & Mondal, S. Comparison and selection of suitable materials applicable for gas turbine blades. *Mater. Today: Proc.* **46**, 8864–8870 (2021).
4. Rui, S. et al. Long-term service induced mechanical properties change of hot-end welding metals in a retired CrMoV bainitic gas turbine rotor. *Mat. Sci. Eng. A* **833**, 142323 (2022).
5. Sankar, V. et al. Optimized thermal barrier coating for gas turbine blades. *Mater. Today: Proc.* **11**, 912–919 (2019).
6. Xiao, Y. Q., Liu, Z. Y., Zhu, W. & Peng, X. M. Reliability assessment and lifetime prediction of TBCs on gas turbine blades considering thermal mismatch and interfacial oxidation. *Surf. Coat. Technol.* **423**, 127572 (2021).

7. Yang, Y. Q. et al. Synergistic effect of multiple molten salts on hot corrosion behaviour of Ni-based single crystal superalloy. *Corros. Sci.* **204**, 110381 (2022).
8. Hu, S., Finklea, H. & Liu, X. A review on molten sulfate salts induced hot corrosion. *J. Mater. Sci. Technol.* **90**, 243–254 (2021).
9. Rapp, R. A. Hot corrosion of materials: a fluxing mechanism? *Corros. Sci.* **44**, 209–221 (2002).
10. Gurrappa, I. Identification of hot corrosion resistant MCrAlY based bond coatings for gas turbine engine applications. *Surf. Coat. Technol.* **139**, 272–283 (2001).
11. Yuan, K. et al. Hot corrosion of MCrAlY coatings in sulphate and SO<sub>2</sub> environment at 900 °C: Is SO<sub>2</sub> necessarily bad? *Surf. Coat. Technol.* **261**, 41–53 (2015).
12. Wang, J., Dangguo, L. & Tianmin, S. Hot corrosion and electrochemical behavior of NiCrAlY, NiCoCrAlY and NiCoCrAlYTa coatings in molten NaCl-Na<sub>2</sub>SO<sub>4</sub> at 800 °C. *Surf. Coat. Technol.* **440**, 128503 (2022).
13. Mobarra, R., Jafari, A. H. & Karaminezhad, M. Hot corrosion behavior of MCrAlY coatings on IN738LC. *Surf. Coat. Technol.* **201**, 2202–2207 (2006).
14. Wang, Q. et al. Oxidation and hot corrosion behaviors of Mo-doped NiMoAlY alloys at 750 °C. *Corros. Sci.* **201**, 110262 (2022).
15. Yu, M., Dapeng, Z., Jibin, P., Tiancheng, C. & Changsheng, L. Effect of Zr, Ti, Ta and Mo addition on high-temperature oxidation and hot corrosion behavior of NiAlY alloys. *J. Alloy. Compd.* **908**, 164614 (2022).
16. Doolabi, M. S., Ghasemi, B., Sadrnezhad, S. K., Habibollahzadeh, A. & Jafarzadeh, K. Hot corrosion behavior and near-surface microstructure of a “low-temperature high-activity Cr-aluminide” coating on Inconel 738LC exposed to Na<sub>2</sub>SO<sub>4</sub>, Na<sub>2</sub>SO<sub>4</sub> + V<sub>2</sub>O<sub>5</sub> and Na<sub>2</sub>SO<sub>4</sub> + V<sub>2</sub>O<sub>5</sub> + NaCl at 900 °C. *Corros. Sci.* **128**, 42–53 (2017).
17. Chen, Z. et al. Influence of Cr content on hot corrosion and a special tube sealing test of single crystal nickel-base superalloy. *Corros. Sci.* **156**, 161–170 (2019).
18. Wang, Q. M. et al. Hot corrosion behavior of AIP NiCoCrAlY(SiB) coatings on nickel base superalloys. *Surf. Coat. Technol.* **186**, 389–397 (2004).
19. Cai, J., Wei, J., Zu, Z., Guan, Q. & Lyu, P. Comparative hot corrosion performance of arc ion plated NiCoCrAlYSiHf coating in Na<sub>2</sub>SO<sub>4</sub>/NaCl/V<sub>2</sub>O<sub>5</sub>-media via high-current pulsed electron beam. *Mater. Charact.* **191**, 112074 (2022).
20. Sundaresan, C. et al. Comparative hot corrosion performance of APS and Detonation sprayed CoCrAlY, NiCoCrAlY and NiCr coatings on T91 boiler steel. *Corros. Sci.* **189**, 109556 (2021).
21. Dong, X., Luo, X., Ge, Y. & Li, C. Enhancing the hot-corrosion resistance of atmospheric plasma sprayed Ni-based coatings by adding a deoxidizer. *Mater. Des.* **211**, 110154 (2021).
22. Jafari, R. & Esmail, S. High-temperature corrosion performance of HVOF-sprayed NiCr, NiAl, and NiCrAlY coatings with alkali sulfate/chloride exposed to ambient air. *Corros. Sci.* **160**, 108066 (2019).
23. Hao, E. et al. Influence of molten salt with or without V<sub>2</sub>O<sub>5</sub> on hot corrosion and high-temperature tribological performance of HVOF-sprayed Ni-based self-lubricating composite coating. *Surf. Coat. Technol.* **417**, 127210 (2021).
24. Wang, H. et al. Hot corrosion behaviour of low Al NiCoCrAlY clad coatings reinforced by nano-particles on a Ni-base super alloy. *Corros. Sci.* **52**, 3561–3567 (2010).
25. Park, K. et al. Degradation characteristics of thermal barrier coatings for hot corrosion and CaO–MgO–Al<sub>2</sub>O<sub>3</sub>–SiO<sub>2</sub>. *Surf. Coat. Technol.* **412**, 127045 (2021).
26. Fan, J. et al. In-situ reaction synthesis Al<sub>2</sub>O<sub>3</sub> overlay modified 7YSZ TBC for NaCl hot corrosion. *Cera. Int.* **47**, 22404–22415 (2021).
27. Pejman, Z. et al. Hot corrosion resistance of Al<sub>2</sub>O<sub>3</sub> nanoparticles reinforced CoNiCrAlY coatings deposited by LPPS and HVOF processes in molten Na<sub>2</sub>SO<sub>4</sub>-V<sub>2</sub>O<sub>5</sub> at 850 °C. *Surf. Coat. Technol.* **472**, 129949 (2023).
28. Sung, P. K. & Poirier, D. R. Estimation of densities and coefficients of thermal expansion of solid Ni-base superalloys. *Mat. Sci. Eng.: A* **245**, 135–141 (1998).
29. Zhao, Z. et al. (Y<sub>0.25</sub>Yb<sub>0.25</sub>Er<sub>0.25</sub>Lu<sub>0.25</sub>)<sub>2</sub>(Zr<sub>0.5</sub>Hf<sub>0.5</sub>)<sub>2</sub>O<sub>7</sub>: A defective fluorite structured high entropy ceramic with low thermal conductivity and close thermal expansion coefficient to Al<sub>2</sub>O<sub>3</sub>. *J. Mater. Sci. Technol.* **39**, 167–172 (2020).
30. Taylor, T. A. & Walsh, P. N. Thermal expansion of MCrAlY alloys. *Surf. Coat. Technol.* **177–178**, 24–31 (2004).

## ACKNOWLEDGEMENTS

This project is financially supported by the National Natural Science Foundation of China under Grant (51671053 and 51801021), the National Key R&D Program of China under Grant (No. 2017YFB0306100), the Fundamental Research Funds for the Central Universities (No. N2102015 and No. N2202019), and by the Ministry of Industry and Information Technology Project (No. MJ-2017-J-99) and the China Postdoctoral Science. Foundation (2022M720674).

## AUTHOR CONTRIBUTIONS

W.Q. and Z.C. have the same contribution to this paper. They conceived the study and directed the research project. W.Q. drafted the manuscript. All authors analyze the data review, and edit the manuscript.

## COMPETING INTERESTS

The authors declare no competing interests.

## ADDITIONAL INFORMATION

**Supplementary information** The online version contains supplementary material available at <https://doi.org/10.1038/s41529-023-00411-z>.

**Correspondence** and requests for materials should be addressed to Zehao Chen or Minghui Chen.

**Reprints and permission information** is available at <http://www.nature.com/reprints>

**Publisher's note** Springer Nature remains neutral with regard to jurisdictional claims in published maps and institutional affiliations.



**Open Access** This article is licensed under a Creative Commons Attribution 4.0 International License, which permits use, sharing, adaptation, distribution and reproduction in any medium or format, as long as you give appropriate credit to the original author(s) and the source, provide a link to the Creative Commons licence, and indicate if changes were made. The images or other third party material in this article are included in the article's Creative Commons licence, unless indicated otherwise in a credit line to the material. If material is not included in the article's Creative Commons licence and your intended use is not permitted by statutory regulation or exceeds the permitted use, you will need to obtain permission directly from the copyright holder. To view a copy of this licence, visit <http://creativecommons.org/licenses/by/4.0/>.

© The Author(s) 2024